Catalysis Today 438 (2024) 114811

Contents lists available at ScienceDirect

Catalysis Today

journal homepage: www.elsevier.com/locate/cattod

Enhanced activity and durability of Pt nanoclusters catalyst by using nitrogen-doped carbon layer coated carbon nanotubes as anchors and nanowires for ORR

Hongwei Zhao [a,b], Yiqing Chen [b,*], Huaiyang Zuo [a], Lin Li [b], Lixiang Li [a], Fangfang Ai [b], Zheyan Tang [a], Tianyu Xing [a,c], Yanqiu Zhang [a], Lin Tao [a], Zhaowen Tian [a], Haiming Yang [a], Xin Geng [a], Baigang An [a,*]

[a] Key Laboratory of Energy Materials and Electrochemistry Research Liaoning Province, School of Chemical Engineering, University of Science and Technology Liaoning, 185 Qianshanzhong Road, Anshan 114051, China
[b] State Key Laboratory of Metal Material for Marine Equipment and Application, Anshan 114009, China
[c] Huizhou (Yussen) Boeko Materials Co. LTD, Huizhou 516300, China

ARTICLE INFO

Keywords:
Fuel cell
Oxygen reduction reaction
Catalytic durability
Pt nanoclusters
N-doped carbon nanotube

ABSTRACT

Platinum-based catalysts remain the top choice for oxygen reduction reaction (ORR) in fuel cells. However, their activity and durability in the acidic medium are still under improvement. In this work, the Pt nanoclusters anchored the nitrogen-doped carbon nanotubes (Pt-NCNTs) have been synthesized by using a series process of pyrrole coating on the CNTs and subsequent pyrolysis to the chemical immersion reduction of Pt ions. The inner CNTs of Pt-NCNTs function as the nanowires offering a high-speed pathway for electron transport, and the Pt nanoclusters increases the active sites. The theoretical calculation demonstrates that the local structural defects and the uneven charge distribution induced by nitrogen-containing functional groups and porous structure are favorable to capture Pt ions for the nucleation of Pt nanoclusters. Compared with the commercial 40 wt% Pt/C (0.94 and 0.80 V), the Pt-NCNTs-1000 with Pt loading amount of 33.0 wt% owns the more positive onset potential and half-wave potential of 0.97 and 0.81 V in the sulfuric acid medium. Meanwhile, the strong attachment of Pt nanoclusters on the nitrogen-doped porous carbon layer results in a stable interface to effectively prevent the metallic species from migration and agglomeration during the electrode reactions. Therefore, the ORR current of Pt-NCNTs-1000 retained 84.3% of the initial value after 50000 s operation superior to the commercial Pt/C (64.6%).

1. Introduction

Proton exchange membrane fuel cells (PEMFCs) are gaining widespread attention for their efficient energy conversion, low operation temperatures, and eco-friendliness [1–3]. However, the sluggish kinetics of oxygen reduction reaction (ORR) at the cathode become a significant barrier for commercialization. A various materials have been developed to enhance the kinetic and efficiency of ORR [4–10]. Among these materials, platinum-based surface stands out as the most active and durable catalysts for ORR in acidic environments. Regrettably, Pt-based catalysts still suffer from the drawbacks of high cost, Pt dissolution in acidic conditions, Ostwald ripening and particle detachment, resulting the limited durability. Consequently, the current research on Pt-based catalysts in acidic environments focuses on two key aspects. One aspect involves enhancing the utilization of catalytic active sites while reducing Pt content for cost reduction. The other aspect focuses on optimizing the interaction between Pt and the support to decelerate Pt migration and aggregation during ORR for durability [11–13].

Reducing the size of Pt catalysts can increase the likelihood of protons, O_2, and electrons coming into contact with the surface, thereby promoting the electrochemical reactions to utilize the active sites [14–16]. However, Pt nanoclusters (Pt NCs) must be strongly anchored to prevent their agglomeration and detachment from the carbon supports for long-cycled activity. To optimize the physical-chemical properties of carbon supports including a high specific surface area, well-defined pore structure, and abundant surface functional groups,

* Corresponding authors.
E-mail addresses: chenyiqing@ansteel.com.cn (Y. Chen), baigang73@126.com (B. An).

https://doi.org/10.1016/j.cattod.2024.114811
Received 27 February 2024; Received in revised form 26 April 2024; Accepted 11 May 2024
Available online 13 May 2024

has emerged as an effective strategy to downsize Pt and enhance the stability of catalysts. Xia et al. utilized the galvanic reaction between a Pt precursor and an amorphous Se film, to prepare the well-dispersed Pt NCs on the carbon support. Meanwhile, the Pt NCs can be securely anchored to the carbon support through Pt-Se-C linkages. The resulted catalyst exhibited strong interaction of metal-support and good durability [17]. Zhou et al. used the porous COF-derived carbon to anchor Pt atoms and nanoclusters. The catalysts as prepared ultimately catalyzed the ORR with high activity and exceptional stability in acidic conditions [18].

Porous carbons are typically used to enhance and enlarge the electrochemical area and the conductivity of catalysts. Consequently, a suitable porous carbon support is of paramount importance [19]. Carbon nanotubes (CNTs) are frequently employed as catalysts support owing to the one-dimensional structure with good conductivity [20–24]. However, the inert surface of CNTs generally leads to weak interfacial interactions with metal catalysts. Therefore, surface modifications introducing functional groups are needed to create strongly anchor sites. Although post-treated or heteroatom-doped CNTs bring a more active surface to strengthen the interactions with catalysts, it also damages the characteristic structure of CNTs to decrease the conductivity [25–27]. Therefore, it still is a challenge to firmly anchor Pt NCs without affecting the intrinsic structure of CNTs. Comparing with post-treatment and the direct doping heteroatoms into the CNTs, coating the polymer containing nitrogen on the CNTs, such as polypyrrole, followed by heat treatment in an inert atmosphere to convert the polypyrrole into nitrogen-containing carbon layers, resulting in CNTs encapsulated by nitrogen-doped carbon layers (NCNTs). This treatment not only introduces nitrogen-containing functional groups into the outer carbon layers, enhancing its surface properties but also preserves the original graphitized structure of the internal CNTs, ensuring superior electron transport capabilities. Moreover, the nitrogen atoms in the nitrogen-doped porous carbon layers of the CNTs significantly enhance the catalytic performance of ORR. The NCNTs is consisted of the inner CNTs and the outer N-doped porous carbon layer (NPCL). The NPCL derives from the conversion of pyrroles, and thus the thickness of NPCL can be controlled at less than 10 nm. Such thin and porous N-doped carbon layer can improve the deposition and utilization of Pt NCs. On the other hand, the inner CNTs with high graphitization can act as a good electronic conductor for the electrons transfer during the reaction. Meanwhile, the nitrogen-containing functional groups and the abundant micropores can enhance the interaction between the carbon matrix and Pt NCs to improve the durability of catalyst.

In this study, the Pt-loaded NCNTs (Pt-NCNTs) was prepared through the pyrolysis of pyrrole coating and chemical immersion reduction of H_2PtCl_6. The nitrogen groups and the abundant micropores within the carbon layer induce electronic structure modifications to enhance the strong interaction between Pt NCs and carbon support. Compared with commercial 40 wt% Pt/C catalysts, Pt-NCNTs-1000 with Pt content of 33.0 wt% exhibits an excellent durability with an impressive 84.3% retention ratio of the current density after continuous operation of 50000 s, which could be attributed to that nondestructive CNTs function as electron nanowires to maintain a high rate electron transfer and strong attachment of Pt NCs onto the N-doped porous carbon layers prevents Pt NCs from the migration and agglomeration during continuous electrode reactions.

2. Experimental

2.1. Chemicals and regents

Carbon nanotubes (CNTs) were obtained from the Institute of Metal Research, Chinese Academy of Science. 40.0 wt% Pt/C catalyst was obtained from Johnson Matthey, the United States. Pyrrole (C_4H_5N, ≥ 99.8%), Ammonium Persulfate ($(NH_4)_2S_2O_8$, ≥ 99.7%), Hydrochloric acid (HCl, 1 M), Dihydrogen hexachloroplatinate (IV) hexahydrate ($H_2PtCl_6{\cdot}(H_2O)_6$, ≥ 99.7%), Sodium borohydride ($NaBH_4$, ≥ 99.7%), Sulfuric acid (H_2SO_4, ≥ 99.7%), and Sodium hydroxide (H_2SO_4, ≥ 95.0%) were obtained from Sinopharm Chemical Reagent Co., Ltd. Ultrapure N_2 and O_2 were supplied by the Anshan Angang gas Limited Liability Company. All the aqueous solutions were prepared with ultrapure water supplied by an ultrapure water system.

2.2. Synthesis of the NCNTs, Pt-NCNTs, Pt-CNT and Pt-NPCs

The NCNTs were synthesized via an in-situ polymerization process involving pyrroles on the CNTs. Subsequently, the resulting polypyrrole-coated CNTs (PPy@CNTs) underwent treatment in an inert atmosphere to transform the PPy coating into nitrogen-doped porous carbon layers [28]. The PPy@CNTs underwent a heat treatment process in a horizontal furnace under pure N_2 gas, following the specified heating procedure. Initially, the sample was heated to 400°C with a heating rate of 4 °C min^{-1} and held at this temperature for 2 h. Subsequently, the temperature was increased to the target value of 600, 800, and 1000 °C, respectively, at a rate of 4 °C min^{-1}, and maintained at this temperature for an additional 2 h. The final samples are marked as NCNTs-600, NCNTs-800, and NCNTs-1000.

Pt-NCNTs were synthesized using the chemical immersion reduction technique. Initially, 50.0 mg of NCNTs (NCNTs-600, NCNTs-800, and NCNTs-1000) were dispersed in 50 mL of ethanol using ultrasonication. Subsequently, a solution of 0.01 M H_2PtCl_6 (13.0 mL) was added to the dispersion. The pH of the solution was adjusted to a pH value of 8.0–9.0 using a 0.1 M NaOH solution, and the mixture was stirred at 0 °C for 4 h. The platinum salt solution containing NCNTs was then heated to 80 °C. The excess 0.01 M $NaBH_4$ solution was slowly added to initiate the reduction reaction of H_2PtCl_6. The reaction proceeded for 4 h with magnetic stirring. The expected Pt content in the sample was 33.6 wt%. Finally, the solution was filtered and washed with deionized water several times. The resulted solid product was dried at 80 °C for 12 h in a vacuum, which was referred to as Pt-NCNTs-600, Pt-NCNTs-800, and Pt-NCNTs-1000.

As the comparison samples, Pt-loaded CNTs (Pt-CNTs) and Pt-loaded nitrogen-doped porous carbons (Pt-NPCs) were synthesized by a similar method. Pt-CNTs were synthesized using the chemical immersion reduction technique. Initially, 50.0 mg of original CNTs were dispersed in 50 mL of ethanol using ultrasonication. The subsequent synthesis was similar to that of Pt-NCNTs. The final sample is marked as Pt-CNTs. Pt-loaded nitrogen-doped porous carbon (Pt-NPCs) were synthesized using direct polymerization without CNTs [28], heat treatment, and chemical immersion reduction technique. Initially, 50.0 mg of nitrogen-doped porous carbons by 1000 °C carbonization directly from polypyrrole was dispersed in 50 mL of ethanol using ultrasonication. The subsequent synthesis was similar to that of Pt-NCNTs. The final sample is marked as Pt-NPCs.

2.3. Structural characterization

Scanning electron microscopy (SEM, FEI Apreo, operated at 1 kV) was employed for morphological analysis. Transmission electron microscopy (TEM, FEI Tecnai G2 F30, operated at 200 kV) provided detailed structural information. Powder X-ray diffraction (XRD, X'pret Powder, Rigaku D/MAX-2500X, Cu Kα) was used to examine crystalline properties. Raman spectrometry (HORIBA Xplora Plus, excited by a 532 nm laser) offered insights into vibrational modes. X-ray photoelectron spectroscopy (XPS) was recorded using a SHIMADZU AXIS SUPRA surface analysis system with Al Kα radiation. Calibration of binding energy positions was achieved using C 1 s at 284.6 eV from the carbon tape. Deconvolution of the N 1 s spectra was performed via a non-linear least squares fitting program with a symmetric Gaussian function. N_2 adsorption-desorption isotherms were measured at −196 °C using a volumetric adsorption analyzer (Micromeritics, ASAP2020). The specific surface area (SSA) was determined using the Brunauer-Emmett-

Teller (BET) method within a relative pressure range of 0.05–0.30. Pore size distribution (PSD) plots were generated based on the adsorption branch of the isotherm, utilizing the nonlocal density functional theory (NLDFT) model. CO_2 adsorption measurements were conducted at 0 °C and various pressures (0–100 kPa) with 20 mg samples. Pt loading amounts were estimated through thermogravimetric analysis (TGA) performed on a TA-DTG-Q600 system in an air atmosphere with a flow rate of 100 mL min^{-1} and a ramp rate of 10 °C min^{-1}.

2.4. Electrochemical tests

All the electrochemical measurements were performed by using a three-electrode electrolytic cell, in which a saturated calomel electrode (SCE) and a platinum plate were used as reference electrode and counter electrode, respectively, a glass carbon electrode (GCE) and a rotating disc electrode (RDE, 0.1256 cm^2) covered with the catalysts were used as the working electrodes. The GCE and RDE were polished by using the slurry of alumina (Al_2O_3, 0.3 and 0.05 μm), then rinsed with ethanol and deionized water in an ultrasonic bath to remove any alumina residues. The catalyst ink was prepared by ultrasonic dispersing 5.0 mg of catalyst powders in 0.5 mL ethanol and 0.5 mL deionized water, into which 50 μL of 5.0 wt% Nafion solution (DuPont) was added, and the suspension as prepared was ultrasonically dispersed to get the homogenous solution. A quantity of 10 μL of the catalyst ink was pipetted out and dropped on the top surface of GCE and RDE. Finally, the electrodes coated with the catalyst ink were dried at room temperature. The electrolyte used for the electrochemical test was 0.5 M H_2SO_4 aqueous solution. Before electrochemical measurements, the working electrodes were immersed in the electrolyte for 2 h. All the potentials reported in this work were referenced to the reversible hydrogen electrode (RHE), $E_{RHE} = E_{SCE} + 0.059\ pH + 0.244$. An electrochemical analysis system (Refernce3000, Gamry) was used to finish electrochemical measurements. The electrochemical impedance spectroscopy (EIS) measurements were performed with a frequency range from 5×10^5 to 0.1 Hz and an amplitude of 10 mV. The ORR performance of catalysts was studied by cyclic voltammetry (CV) and linear scan voltammetry (LSV) measurements. CVs were recorded at a scan rate of 50 mV s^{-1}. LSVs were measured at a scan rate of 10 mV s^{-1} under rotation speeds of 400, 625, 900, 1225, 1600, 2025, and 2500 rpm. The electrolyte was purged with pure N_2 or O_2 gas (for at least 30 min) before electrochemical tests. The slopes of their linear-fit lines were used to calculate the number of electrons transferred per oxygen molecule (n) based on the Koutecky-Levich (K-L) equation [29]:

$$\frac{1}{J} = \frac{1}{J_K} + \frac{1}{J_L} = \frac{1}{J_K} + \frac{1}{B\omega^{1/2}}$$

$$B = 0.\quad 2nFC_0D_0^{2/3}\upsilon^{-1/6}$$

$$J_K = nFkC_0$$

In the equations, J, J_K, and J_L are the measured current density, kinetic current density, and limiting diffusion current density, respectively. ω is the angular velocity of disk rotation rates, n is the total electron transfer number of ORR, and F (96485 C mol^{-1}) is the Faraday constant. In the 0.5 M H_2SO_4 solution, the bulk concentration of oxygen is C_0 (1.9×10^{-5} cm^2 s^{-1}), the diffusion coefficient of O_2 is D_0 (1.2×10^{-6} mol cm^{-3}) and ν is the kinematic viscosity of the electrolyte (0.01 cm^2 s^{-1}) [29].

For RRDE tests, the electrochemical workstation CHI 760E was employed the disk electrode (0.2475 cm^2) was scanned catholically at a rate of 10 mV s^{-1}, and the ring electrode (0.1866 cm^2) potential was set to 1.23 V vs. RHE. The H_2O_2 yield (% H_2O_2) and electron transfer number (n) are determined by using the following equations [29]:

$$\%H_2O_2 = 200\frac{I_R/N}{I_D + I_R/N}$$

$$n = 4\frac{I_D}{I_D + I_R/N}$$

where N is the current collection efficiency of the ring electrode (N=37% in this article), I_R is the ring current and I_D is the disk current.

2.5. Density functional theory (DFT) calculations

The structural optimization and electronic property calculations for pristine pure CNT, the N-doped model of CNT, and the micropore model of CNT were all carried out using DFT (Density Functional Theory) with the Dmol^3 code [30]. Under the Perdew−Burke−Ernzerhof functional, the method of generalized gradient approximation was utilized to define the exchange−correlation interaction. The double numerical basis set with a polarization function was employed to handle atomic orbitals. Additionally, we utilized a dispersion-corrected DFT (DFT-D) method was utilized the Grimme vdW correction, which can accurately describe weak interactions in all calculations. The real-space global cutoff radius was set at 4.9 Å, and we employed a Monkhorst−Pack scheme with 3×2×1 k-points to ensure high-quality theoretical evaluations across the Brillouin zone. In addition, during geometry optimizations, we applied convergence tolerances of 1×10^{-5} Ha for the total energy, 0.002 Ha/Å for atomic forces, and 0.005 Å for the highest displacement. The electron distribution and charge transfer were determined using the Mulliken method.

3. Results and discussion

As illustrated in Fig. 1, the polypyrrole was uniformly coated on the outer surface of CNTs by in-situ polymerization. Pyrolysis of polypyrrole at 1000 °C in N_2 atmosphere resulted the formation of nitrogen-doped porous carbon layers to get the NCNTs-1000. Subsequently, the NCNTs-1000 were introduced into a pre-prepared H_2PtCl_6 solution at 0 °C. A chemical immersion reduction process was then employed by utilizing a $NaBH_4$ aqueous solution as the reductant, which led to the formation of a quantity of Pt nanoclusters (Pt NCs) uniformly anchoring onto the NCNTs. As an illustration, it was imagined that CNTs can act as electronic nanowires to enhance the charge transfer. and the external porous nitrogen-doped carbon layers containing a variety of functional groups can serve as robust nucleation sites to strengthen the interaction between Pt NCs and the carbon support, thereby an efficient and stable ORR can be obtained by using Pt-NCNT-1000 as catalyst.

The morphological changes from the CNTs to the Pt-NCNTs-1000 were documented using SEM (Fig. 2a-c), and SEM images of other samples are shown in Fig. S1. It is worth noting that the diameter and surface roughness of the NCNTs-1000 (Fig. 2b) is greater than the CNTs (Fig. 2a) attributing to the nitrogen-doped porous carbon layer derived from the transformation of polypyrrole coating. The morphology of NCNTs-600 and NCNTs-800 (Fig.S1a-b) resembles that of NCNTs-1000, suggesting that the heat treatment temperature exerts minimal influence on the macroscopic morphology of samples. In the Pt-NCNTs-1000 (Fig. 2c), a substantial Pt NCs are uniformly dispersed on the surface of NCNTs-1000 and there is no significant agglomeration of Pt NCs. In comparison, Pt-NCNTs-600 and Pt-NCNTs-800 (Fig. S1c-d) exhibit a significant clustering of Pt NCs, which is attributed to the changes in porosity and types of nitrogen-containing functional groups in the outer nitrogen-doped carbon layers. As shown in Fig. S1e-f, the inert surface of the CNTs in Pt-CNTs resulted much larger Pt particles deposited on the CNTs. The large size of NPCs in Pt-NPCs caused the random distribution of Pt particles around NPCs. In addition, the element mapping results from the SEM analysis of Pt-NCNTs-1000 are depicted in Fig S2, which shows that both nitrogen (N) and platinum (Pt) elements are uniformly distributed in the Pt-NCNTs-1000.

The TEM analyses of Pt-NCNTs-1000 are shown in Fig. 2d, it is evident that the Pt NCs are densely loaded and evenly distributed within

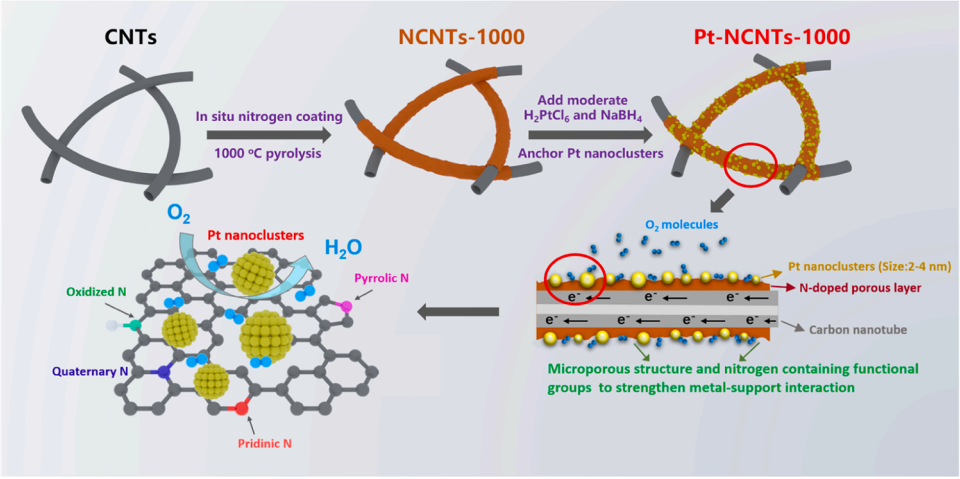

Fig. 1. Schematic synthesis structure of Pt-NCNTs-1000.

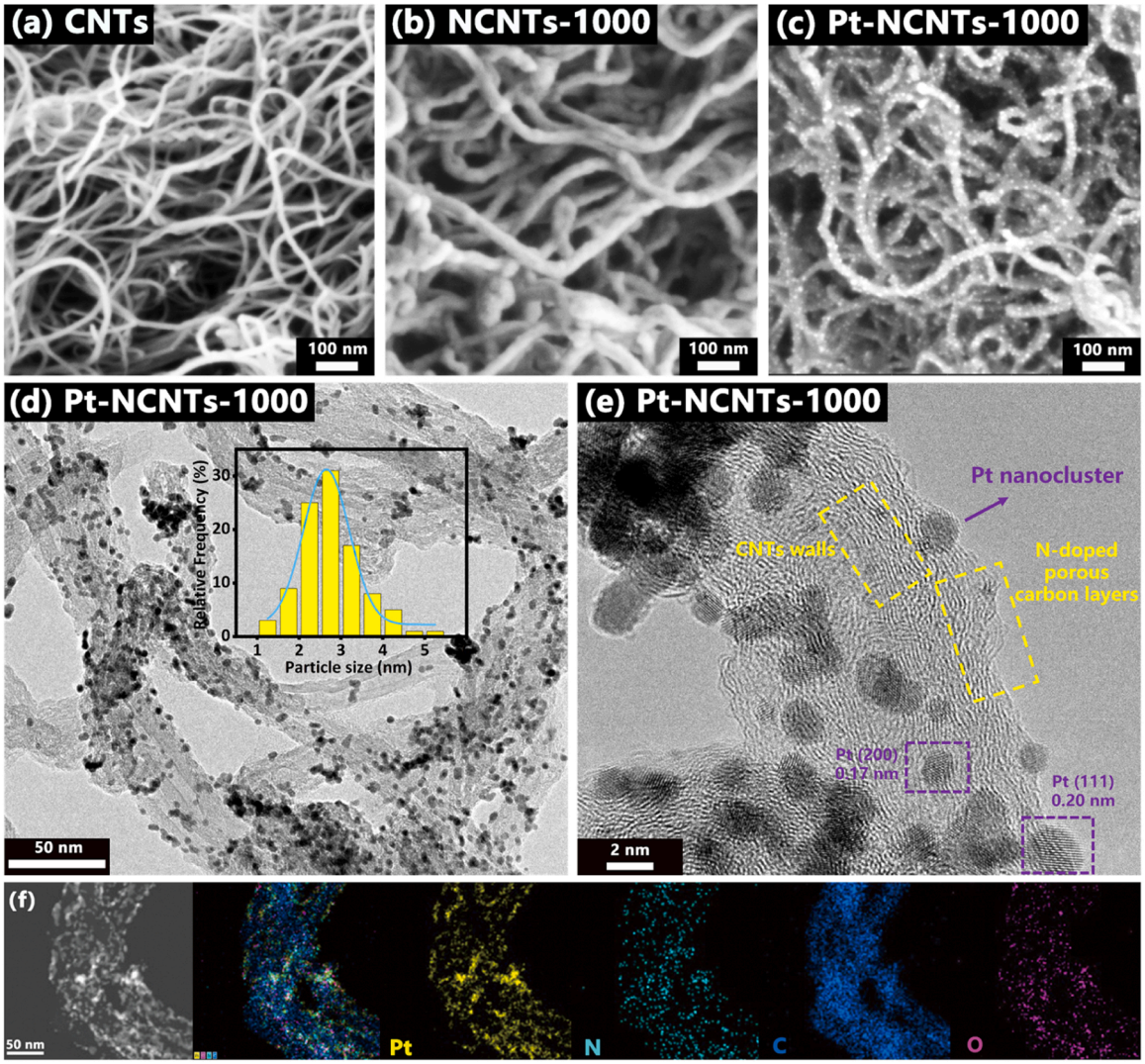

Fig. 2. SEM image of (a) CNTs, (b) NCNTs-1000, (c) Pt-NCNTs-1000. (d) TEM and (e) HRTEM image of Pt-NCNTs-1000. (f) EDX elemental maps of Pt-NCNTs-1000: Pt (yellow), N (light blue), C (blue) and O (pink). The inset represents a histogram of the particle sizes (diameters) found in the (d) TEM image.

the NCNTs. The predominant size falls between 2 and 4 nm, as indicated by the histogram. HRTEM image (Fig. 2e) reveals the robust anchoring of Pt NCs on the surface of NCNTs with discernible lattice spacings of 0.20 and 0.17 nm corresponding to the (111) and (200) crystallographic planes of metallic Pt. Meanwhile, the inner CNTs exhibit clearly defined lattice fringes signifying a high degree of graphitization, which can function as good electronic nanowires to transfer the charges during electrochemical reactions. Fig. 2f displays the high-angle annular dark-field scanning transmission electron microscopy (HAADF-STEM) image and corresponding EDS element mappings of Pt-NCNTs-1000. The uniformly distributed and randomly scattered dots indicate that Pt nanoclusters are highly dispersed within NCNTs. Additionally, element mappings were performed to visualize the distribution of Pt, N, C, and O elements in Fig. 2f, confirming that these elements aligns well with the nanostructure's profile.

X-ray powder diffraction (XRD) was used to defect the crystal phases of samples. As depicted in Fig. 3a, all the samples exhibit a diffraction peak at 2θ of 26.2° corresponding to the (002) plane of carbon [31]. The diffraction peaks at 2θ of 39.8°, 46.3°, 64.5°, and 81.6° correspond to the crystalline planes of (111), (200), (220), and (311) of Pt, respectively [32]. Raman spectroscopy is a reliable method to assess the graphitization degree of materials. The samples of CNTs, NCNTs-1000, and Pt-NCNTs-1000 (Fig. 3b) present the graphitic peak (G band) at 1600 cm^{-1}, the peak associated with structural defects (D band) at 1340 cm^{-1}, a peak attributed to amorphous carbon (Am band) at 1515 cm^{-1}, and a peak corresponding to sp^3-bonded carbon atoms (P band) at 1200 cm^{-1} (Fig. 3c and S3) [33]. The relative intensity ratio of the D and G bands (I_D/I_G) is directly related to the defects in the graphitic carbon structure. The I_D/I_G value (1.19) of Pt-NCNTs-1000 is higher than CNTs (0.85) and NCNTs-1000 (1.02), signifying a great number of defects in graphitic structure, which resulted by the abundant pores and nitrogen-containing functional groups in the outer nitrogen-doped carbon layers of NCNTs. The Pt content in Pt-NCNTs-1000 was determined to be approximately 33.0 wt% by TGA (Fig. 3d), which is slightly higher than Pt-NCNTs-600 (31.5 wt%) and Pt-NCNTs-800 (32.3 wt%) (Fig. S4). According to the chemical reaction, the theoretical value of Pt amount on the NCNT-1000 is 33.6 wt%, it indicates that the stronger anchoring between Pt and NCNTs-1000 almost resulted all of the Pt NCs being stably deposited onto the NCNTs-1000.

To further investigate the interactions between Pt NCs and the porous structure of the substrates, N_2 adsorption-desorption measurements were employed to systematically analyze the pore parameters of the samples. Firstly, the adsorption/desorption isotherms of samples exhibit a similar multi-stage adsorption process, ranging from ultra-low pressure to high pressure [34,35]. The adsorption capacity of NCNTs-1000 was significantly higher than CNTs (Fig. 4a) and the other NCNTs samples (Fig. S5a) at P/P_0<0.05. This indicates the formation of the nitrogen-doped porous carbon layers around CNTs. With increasing the heat treatment temperature, the external nitrogen-carbon layer undergoes further contraction, accompanied by the transformation and the loss of nitrogen-containing functional groups, which leads to an enhanced micropore content of the NCNTs. The pore size distribution (Fig. 4b and S5b) further corroborates this transformative process. Notably, NCNTs-1000, characterized by its more porous structure, exhibits the highest specific surface area (SSA) of 281 $m^2\ g^{-1}$, along with superior total pore volume (V_{total}) of 0.22 cm^3/g, micropore volume (V_{micro}) of 0.124 $cm^{-3}\ g^{-1}$, and a micropore to total pore volume ratio (V_{micro}/V_{total}) of 57.9%, surpassing all other samples (Table 1). The adsorption/desorption isotherms and pore size distribution for the

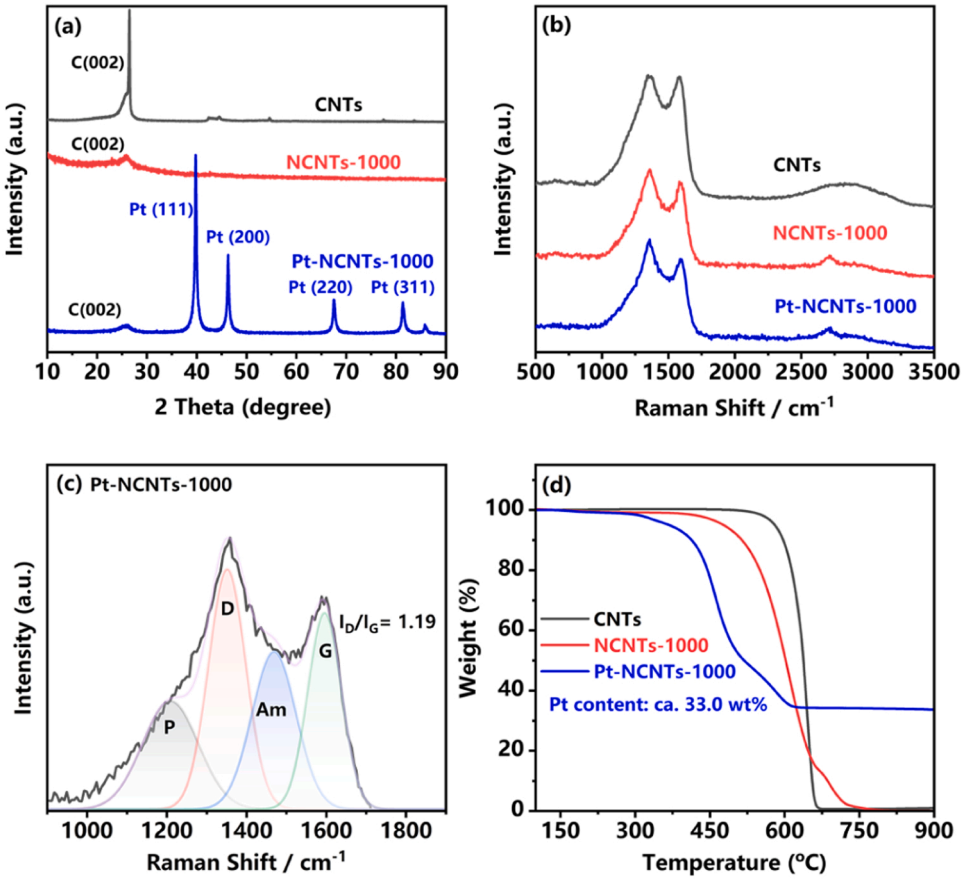

Fig. 3. (a) XRD patterns. (b) Raman spectrums. (c) Deconvoluted components (D, G, P, Am), fitting result, and the values of I_D/I_G of Pt-NCNTs-1000. (d) TGA curves for CNTs, NCNTs-1000, and Pt-NCNTs-1000.

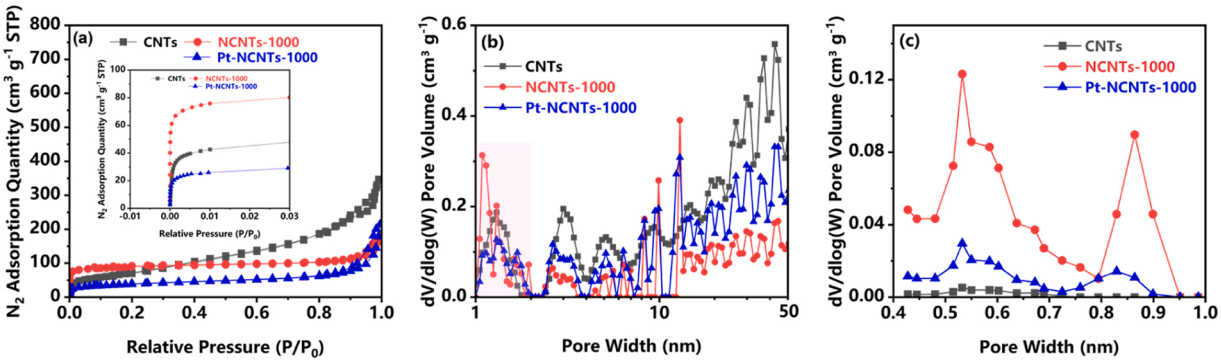

Fig. 4. (a) N_2 adsorption-desorption isotherms. (b) NLDFT pore size distribution (1.0–50.0 nm) derived from N_2 adsorption isotherm. (c) NLDFT pore size distribution (0.4–1.0 nm) derived from CO_2 adsorption isotherm (0 °C).

Table 1
Pore parameters were obtained from the N_2 adsorption-desorption isotherms at −196 °C for the CNTs, NCNTs, and Pt-NCNTs.

Samples	SSA[a] (m^2 g^{-1})	V^b_{total} (cm^3 g^{-1})	V^c_{micro} (cm^3 g^{-1})	V_{micro}/V^d_{total} (%)
CNTs	242	0.83	0.027	3.2%
NCNTs-600	106	0.09	0.039	43.3%
NCNTs-800	189	0.11	0.061	55.5%
NCNTs-1000	281	0.22	0.124	57.9%
Pt-NCNTs-600	87	0.12	0.017	14.2%
Pt-NCNTs-800	127	0.19	0.025	13.1%
Pt-NCNTs-1000	134	0.20	0.039	18.6%

aSSA (specific surface area) was calculated from the adsorption data near 0.05 ≤ P/P0 ≤ 0.35. b Vtotal (total pore volume) and c Vmicro (micropore volume) were determined from the NLDFT cumulative volume in the pore diameter ranges of d ≤ 50 nm and d ≤ 2 nm, respectively. d Vmicro/ Vtotal was the ratio of micropore volume to total pore volume.

different samples of Pt-NCNTs are shown in Fig. S5c-d, the adsorption capacity at $P/P_0<0.05$ and micropore content of Pt-NCNTs are inferior to those observed in the corresponding NCNTs samples, the SSA and pore volume of Pt-NCNTs samples were also significantly reduced (Table 1). Compared to CNTs (Fig. 4b), the content of micropores of NCNTs-1000 and Pt-NCNTs-1000 initially increases and then decreases further suggesting that the microporous structure contributed by the nitrogen-doped porous carbon layer becomes occupied by Pt NCs. Meanwhile, the pore size distribution of 0.4–1.0 nm (Fig. 4c) is derived from CO_2 adsorption isotherms (Fig. S6). These micropores mainly facilitate the more readily capture of $[PtCl_6]^{2-}$ (approximately 0.5 nm in size) [36]. When the nucleation of Pt occurs in such a small limited space (less than 2 nm in diameter), the growth and agglomeration of Pt NCs will be inhibited. Consequently, a large amount of Pt NCs (2–4 nm) can deposit on NCNTs-1000. The smaller Pt NCs strongly anchored onto NCNTs-1000 will expose the larger active surface for ORR to enhance the catalytic activity and durability.

To further elucidate the surface composition of catalyst, XPS measurements were conducted to examine the chemical states of the samples. The XPS survey spectra of samples can be observed in Fig. 5a. There are characteristic peaks at binding energies of 284.5 eV and 532.2 eV, assigned to C 1 s and O 1 s in CNTs, respectively [37,38]. The NCNTs-1000 exhibit N 1 s characteristic peaks at a binding energy of 398.5 eV, confirming the successful introduction of nitrogen atom [37]. The high-resolution N 1 s spectra of NCNTs-1000 (Fig. S7) and Pt-NCNTs-1000 (Fig. 5b) were deconvoluted into four peaks centered at 398.2, 400.1, 401.0, and 402.1 eV, which corresponds to pyridinic-N, pyrrolic-N, quaternary-N, and oxide pyridinic-N, respectively [39]. Previous studies have indicated that both pyridinic-N and quaternary-N play important roles in enhancing ORR activity, albeit through different mechanisms [40,41]. Pyridinic-N has been demonstrated to be responsible for increasing current density, spin density, and the density of π states of the C atoms near the Fermi level. Meanwhile, quaternary-N can serve as an electron donor in nitrogen-doped carbon, facilitating the transport of electrons from neighboring C atoms to Pt species [41]. The contents of various nitrogen atom types were calculated from the N 1 s spectra and are detailed in Table S1. The total nitrogen content and the proportion of different nitrogen-containing functional groups in NCNTs-1000 and Pt-NCNTs-1000 are quite similar, which suggests that the process of Pt NCs loading has little impact on the surface chemical properties of NCNTs. All Pt-NCNTs samples have the characteristic peak of Pt 4 f in the binding energy range of 70–80 eV (Fig. 5c and S8) [42]. The high-resolution Pt 4 f spectrum (Fig. 5c) of Pt-NCNTs-1000 can be fitted into Pt^0 (71.2 eV and 74.6 eV) and Pt^{2+} (72.0 eV and 76.5 eV) peaks, indicating that the Pt NCs are successfully anchored through chemical immersion reduction [41,42]. In Table S2, the Pt content in Pt-NCNTs-1000 (5.6 at%) is higher than in Pt-NCNTs-600 (3.9 at%) and Pt-NCNTs-800 (4.6 at%). This increase is attributed to the Pt-NCNTs-1000 not only has a large specific surface area and substantial micropore volume but also contains abundant nitrogen-containing functional groups. These features significantly enhance the interaction between Pt and NCNTs-1000, resulting in a higher Pt content as well as smaller, more uniformly distributed Pt NCs. To further demonstrate the interaction between Pt and NCNTs, XPS analyses on the Pt-CNTs and Pt-NPCs were performed. The results (Fig. S9) showed that Pt-CNTs contained only 0.8 at% Pt (Table S3). In contrast, the Pt content in Pt-NPCs increased to 2.8 at% due to the introduction of nitrogen-containing functional groups. However, the limited specific surface area and small pore volume constrained Pt deposition in Pt-NPCs. These results confirmed the stronger interaction between Pt and NCNTs.

Furthermore, theoretical calculations can provide another effective method to further substantiate the interaction between Pt and NCNTs. Therefore, based on the pore structure and XPS characterization results, in our work, three computational models (Fig. 5d-f) of type I (pure CNT), II (N-doped model of CNT), and III (micropore model of CNT) were used to theoretically confirm the effects of NCNT. To investigate the anchoring capability of H_2PtCl_6 molecules, the structural optimization of the calculation model was further conducted, and the results are presented in Fig. 5g-i. By calculating the adsorption energy, it is evident that the adsorption capacity of the H_2PtCl_6 molecule on type I is very weak, while the E_{ads} of type II and III are −10.6 and −7.7 eV, respectively, which is higher than that of pure CNT. Furthermore, the analysis of charge density reveals significant charge accumulation and dissipation phenomena of the H_2PtCl_6 molecule on types I and II structures. This observation further confirms that the local structural defects and uneven charge distribution induced by these nitrogen-containing functional groups and porous structure are favorable for capturing H_2PtCl_6, thus creating minimal nucleation sites for Pt NCs.

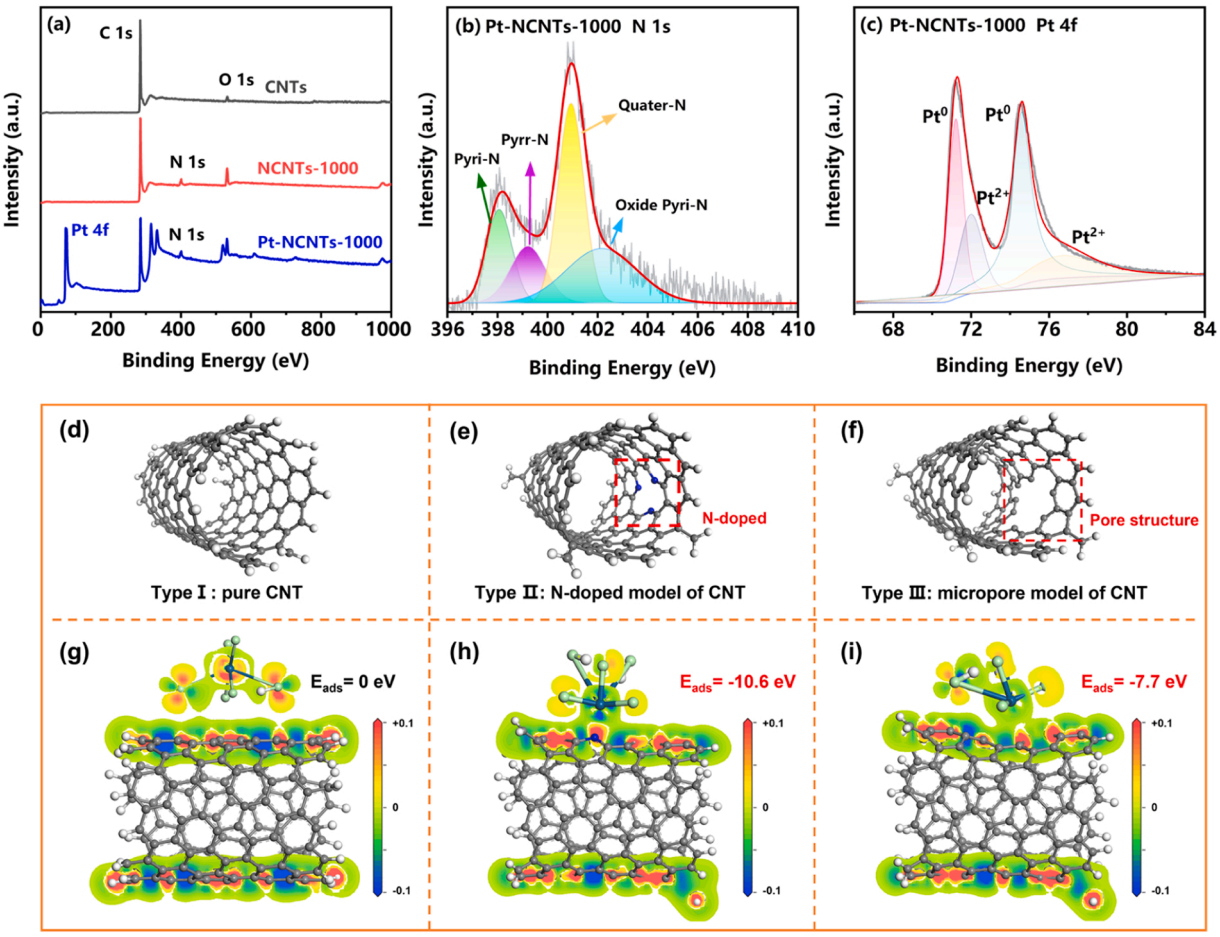

Fig. 5. (a) XPS survey spectra. High-resolution (b) N 1 s and (c) Pt 4 f XPS spectra of Pt-NCNTs-1000. The geometric structure of pure CNT, N-doped model of CNT, and micropore model of CNT. Charge density of (g) pure CNT, (h) N-doped model of CNT, and (i) micropore model of CNT. White, gray, light green, dark blue, and blue spheres represent O, C, Cl, Pt, and N atoms, respectively. Densities are displayed with an isosurface and the interval of isovalue is between −0.1 and 0.1 e/Å^3.

The catalytic performance of NCNTs-1000, Pt-NCNTs-1000, Pt-CNTs, Pt-NPCs, and commercial 40.0 wt% Pt/C toward ORR was initially assessed through CV in an O_2-saturated 0.5 M H_2SO_4 solution. As shown in Fig. 6a. NCNTs-1000 do not exhibit any characteristic peak in the 0.5 M H_2SO_4 solution, signifying its limited ORR catalytic activity. In contrast, both Pt-loaded catalysts display distinct ORR peaks (Fig. 6a and S10). Among these, Pt-NCNTs-1000 demonstrates a more positive peak potential (0.74 V) and higher peak current compared to other samples, closely approximating the performance of Pt/C (0.73 V). LSV curves as shown in Fig. 6b, the Pt-NCNTs-1000 achieves a higher limiting current density (5.4 mA cm^{-2}) than the Pt/C catalyst (4.8 mA cm^{-2}). It also features a notably improved half-wave potential (0.81 V) and onset potential (0.97 V) relative to Pt/C (0.80 V, 0.94 V). Meanwhile, Pt-NCNTs-1000 displays ORR catalytic performance that is significantly superior to that of Pt-CNTs and Pt-NPCs. The Tafel slope of Pt-NCNTs-1000 is 88 mV dec^{-1} (Fig. 6c), which is higher than that of NCNTs-1000 (130 mV dec^{-1}), Pt-CNTs (105 mV dec^{-1}), Pt-NPCs (98 mV dec^{-1}) and Pt/C (97 mV dec^{-1}), suggesting the fast ORR kinetics of Pt-NCNTs-1000.

Electrochemical impedance spectroscopy (EIS) was employed to investigate the electron transfer ability of samples. The Nyquist plots (Fig. 6d) are composed of a semi-circle in the high-frequency region and a nearly straight line in the low-frequency region. The semicircular part is attributed to the electron transfer-limited (kinetic) process, while the linear portion corresponds to the diffusion process. Comparatively, Pt-NCNTs-1000 exhibited a lower charge transfer resistance (R_{ct}) of 1.31 Ω, surpassing that of CNTs (2.81 Ω), NCNTs-1000 (4.85 Ω), Pt-CNTs (8.68 Ω) and Pt-NPCs (3.88 Ω), implying Pt-NCNTs-1000 has efficient electron transfer ability. Although the R_{ct} values of all samples were small, the NCNTs-1000 were slightly higher than the CNTs. This result can be attributed to the increase in defects and porous structure induced by the nitrogen-doped carbon layers, which was verified through Raman and pore structure analysis. However, the R_{ct} of Pt-NCNTs-1000 has decreased to 1.31 Ω, which can likely be attributed to the superior conductivity and even distribution of Pt NCs, which effectively compensates for the electron conduction deficiencies in NCNTs-1000, markedly reducing its R_{ct}. Additionally, the Pt-CNTs experiences the higher resistance owing to lower and uneven Pt NCs loading, and the Pt-NPCs shows the elevated resistance resulting from the absence of CNTs nanowire conductors.

To learn the reaction mechanism of Pt-NCNTs-1000, LSV test was performed at different rotation speeds ranging from 400 to 2500 rpm. Based on LSV (Fig. S11a), the Koutecky-Levich (K-L) diagram of Pt-NCNTs-1000 was plotted, which displays a strong linear relationship at various potentials (Fig. S11b), indicating the first-class dynamics kinetics towards dioxygen fragmentation. The number of electron transfers (n) can be calculated by analyzing the K-L plots of J^{-1} versus $\omega^{-1/2}$. The results show that the n value of Pt-NCNTs-1000 ranges from 3.5 to 3.9 in the potential range of 0.40–0.70 V. RRDE test was also conducted to further get the mechanism information of ORR, and the LSV curves are plotted in Fig. 6e together with the H_2O_2 current detected by the Pt ring electrode at 1.2 V (vs. RHE). In contrast, Pt-NCNTs-1000 has a slightly lower ring current and higher disk current than Pt/C (Fig. 6e inset), indicating that there was almost no formation of intermediate

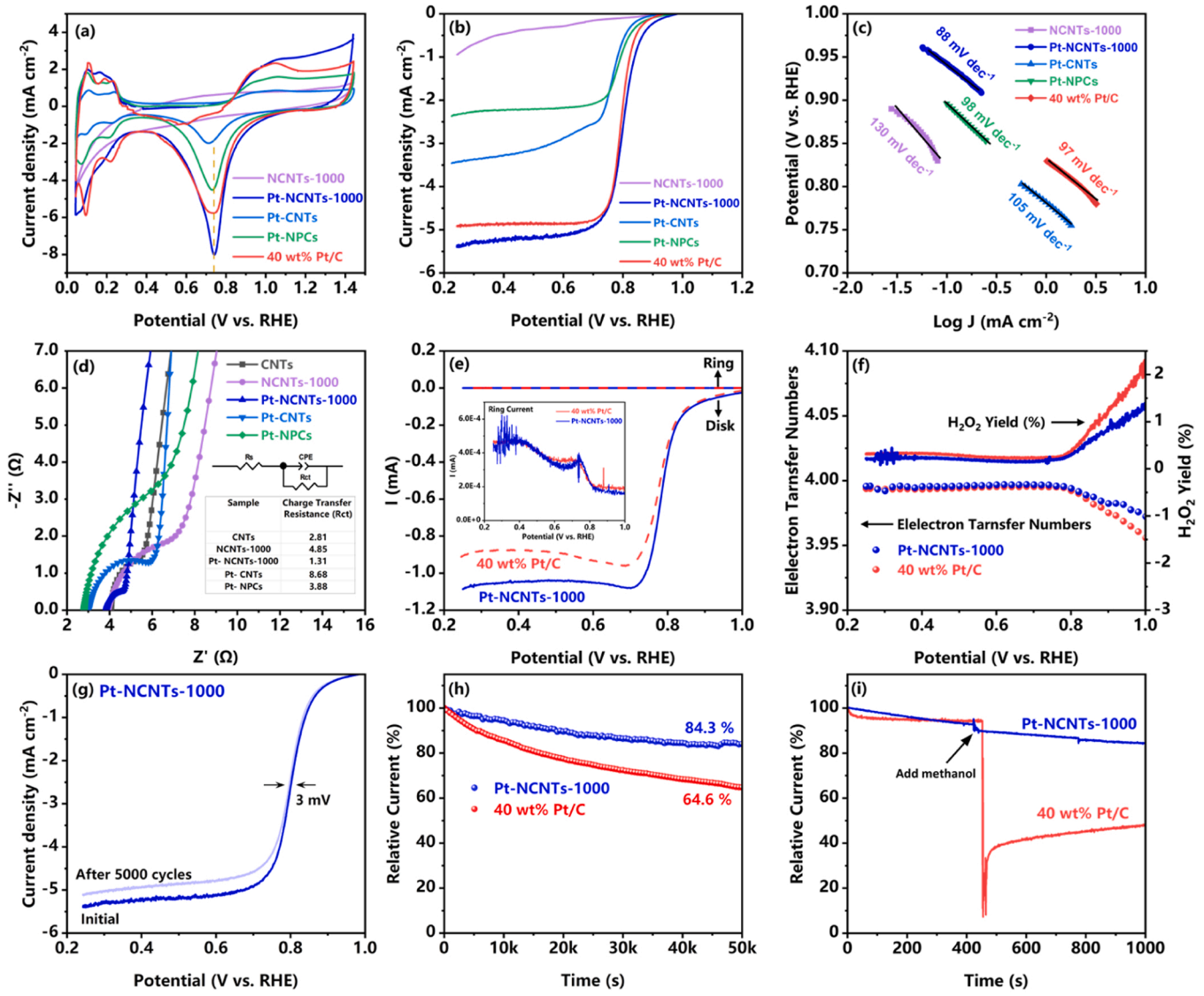

Fig. 6. (a) CV curves recorded in O_2-saturated 0.5 M H_2SO_4 solution. (b) LVS curves and (c) Tafel slopes at a rotation rate of 1600 rpm. (d) EIS measurements, the inset displays the equivalent circuit model for EIS. (e) RRDE voltammetry in O_2-saturated 0.5 M H_2SO_4 solution at a rotation rate of 1600 rpm. The inset in (e) is the magnifying figure of the ring current at 0.2–1.0 V vs RHE. (f) Electron transfer numbers (scatter plot) and peroxide yield (line chart). (g) LSV of Pt-NCNTs-1000 before and after 5000 cycles CV. (h) Chronoamperometric responses at 0.7 V vs. RHE with a rotation rate of 1600 rpm. (i) The Pt-NCNTs-1000 and commercial 40.0 wt% Pt/C were kept at 0.7 V vs. RHE when 10 mL methanol was added at 400 s with a rotation rate of 1600 rpm.

peroxide (H_2O_2) and a large portion of O_2 was directly reduced into H_2O for the Pt-NCNTs-1000. Fig. 6f further shows the *n* value and H_2O_2 yield of samples, the *n* of Pt-NCNTs-1000 remains 3.97–4 for potentials ranging from 0.3 to 0.8 V, similar to Pt/C catalyst, and the H_2O_2 yield of Pt-NCNTs-1000 (0.23%) is lower than that of Pt/C catalyst (0.33%), remains at a consistently low level of less than 1%. This minimal H_2O_2 yield unequivocally confirms the excellent ORR catalytic activity, where O_2 is directly and completely reduced into H_2O via the highly efficient four-electron pathway in acidic conditions. Additionally, compared to Pt-based catalysts reported in some literature (Table S4), Pt-NCNTs-1000 demonstrates good catalytic performance.

The durability is important factor to evaluate the performance of Pt-based catalysts. The accelerating test following 5000 cycles of CV was conducted to evaluate the durability of catalysts. The half-wave potential of Pt-NCNTs-1000 decreases by only 2 mV compared to its initial value (Fig. 6g), however, in the case of Pt/C, it decreases by 20 mV (Fig. S12). Meanwhile, SEM image of Pt-NCNTs-1000 (Fig. S13) reveal that the Pt NCs remain firmly and uniformly anchored to NCNTs even after the 5000 cycles test. The chronoamperometry method (Fig. 6h) was employed to further assess the durability of Pt-NCNTs-1000. After 50000 s, the ORR current of Pt-NCNTs-1000 retains 84.3% of its initial value, which is notably superior to the Pt/C (64.6%). The enhanced durability of Pt-NCNTs-1000 can be attributed to the robust attachment of Pt NCs to the N-doped porous CNTs. This strong attachment is facilitated by the porous anchoring strategy, resulting in a stable interface bond that effectively prevents the metallic species from migration and agglomeration during continuous electrode reactions.

In the PEMFCs systems, CO commonly appears as an impurity during hydrogen production and exhibits a strong affinity to Pt, forming a stable adsorption layer on the Pt surface. CO molecules occupy the active sites of the catalyst, inhibiting interactions with reactants in the fuel cell, such as hydrogen or oxygen. This results in the blockage and reduction of available active sites for catalytic reactions, significantly decreasing catalytic efficiency. Therefore, the resistance of catalysts to chemical interference is particularly crucial. To evaluate this aspect, the ability to resist chemical interference is tested using methanol, which has a different adsorption mechanism but is safer than CO. As shown in Fig. 6i, by using chronoamperometric, Pt-NCNTs-1000 also exhibits

excellent resistance to methanol. The relative current changes slightly after the introduction of methanol for Pt-NCNTs-1000. In contrast, a significant reduction in the relative current is observed for the Pt/C catalyst, and the current cannot be restored to the previous value. The performance differences may be attributed to the uniform distribution of Pt NCs in Pt-NCNTs-1000, which optimizes the utilization efficiency of active catalytic sites. The synergistic effects of nitrogen-doping and small size Pt NCs effectively resist the adsorption and blockage by methanol and its decomposition products, thereby enhancing the resistance of the catalyst to interference.

4. Conclusion

Pt-NCNTs catalyst that loaded with Pt nanoclusters with size of 2–4 nm loaded on the nitrogen-doped porous carbon coated carbon nanotubes (NCNTs) was successfully achieved through a straightforward process involving pyrrole coating, pyrolysis, and chemical immersion reduction. The inner CNTs within Pt-NCNTs function as efficient electronic nanowires to provide a high-speed pathway for electron transport of electrode reactions. The outer nitrogen-doped carbon layers can supply more active and anchor sites for Pt deposition. The theoretical calculation demonstrates that the nitrogen-functionalized groups and porous structure can facilitate a strong anchoring effect for Pt nanoclusters, ensuring uniform growth and distribution of Pt nanoclusters. The Pt-NCNTs-1000 with Pt loading amount of 33.0 wt% owns the more positive onset potential and half-wave potential of 0.97 and 0.81 V in the sulfuric acid medium, comparing with the commercial 40 wt% Pt/C (0.94 and 0.80 V). Furthermore, the strong attachment of Pt nanoclusters to the nitrogen-doped porous carbon results in a stable interface that effectively prevents the migration and agglomeration of metallic species during continuous electrode reactions. After a durability test of more than 50000 s, the ORR current of Pt-NCNTs-1000 retains 84.3% of its initial value, which is notably superior to the commercial 40 wt% Pt/C (64.6%). The present work could provide valuable guidance for designing and constructing highly active and stable Pt-based catalysts.

CRediT authorship contribution statement

Baigang An: Writing – review & editing, Funding acquisition, Conceptualization. **Fangfang Ai:** Formal analysis. **Zheyan Tang:** Data curation. **Lin Li:** Supervision. **Lixiang Li:** Writing – review & editing, Funding acquisition, Conceptualization. **Lin Tao:** Validation, Software. **Zhaowen Tian:** Formal analysis. **Tianyu Xing:** Data curation. **Yanqiu Zhang:** Formal analysis. **Huaiyang Zuo:** Data curation. **Haiming Yang:** Supervision. **Hongwei Zhao:** Writing – original draft, Data curation. **Xin Geng:** Supervision. **Yiqing Chen:** Supervision, Conceptualization.

Declaration of Competing Interest

The authors declare that they have no known competing financial interests or personal relationships that could have appeared to influence the work reported in this paper.

Data availability

Data will be made available on request.

Acknowledgements

We acknowledge the financial support by grants from the National Natural Science Foundation of China (51872131, 51972156, 51672117, 51672118), the Nature Science Foundation of Liaoning Province (2023-BS-184), the University of Science and Technology Liaoning Talent Project Grants (6003000315), and the Joint Fund projects of University of Science and Technology Liaoning State-Key Laboratory of Metal Material for Marine Equipment and Application (HGSKL-USTLN(2022) 10).

Appendix A. Supporting information

Supplementary data associated with this article can be found in the online version at doi:10.1016/j.cattod.2024.114811.

References

[1] F. Xiao, G. Xu, C. Sun, I. Hwang, M. Xu, H. Wu, Z. Wei, X. Pan, K. Amine, M. Shao, Durable hybrid electrocatalysts for proton exchange membrane fuel cells, Nano Energy 77 (2020) 105192, https://doi.org/10.1016/j.nanoen.2020.105192.
[2] K. Jiao, J. Xuan, Q. Du, Z. Bao, B. Xie, B. Wang, Y. Zhao, L. Fan, H. Wang, Z. Hou, S. Huo, N.P. Brandon, Y. Yin, M.D. Guiver, Designing the next generation of proton-exchange membrane fuel cells, Nature 595 (2021) 361–369, https://doi.org/10.1038/s41586-021-03482-7.
[3] F. Xiao, Y. Wang, Z. Wu, G. Chen, F. Yang, S. Zhu, K. Siddharth, Z. Kong, A. Lu, J. Li, C.J. Zhong, Z. Zhou, M. Shao, Recent advances in electrocatalysts for proton exchange membrane fuel cells and alkaline membrane fuel cells, Adv. Mater. 33 (2021) 2006292, https://doi.org/10.1002/adma.202006292.
[4] Y. Wang, D. Wang, Y. Li, A fundamental comprehension and recent progress in advanced Pt-based ORR nanocatalysts, SmartMat 2 (2021) 56–75, https://doi.org/10.1002/smm2.1023.
[5] L. Wu, S.X. Li, L.X. Li, H. Zhang, L. Tao, X. Geng, H.M. Yang, W.M. Zhou, C.G. Sun, D.Y. Ju, B.G. An, Modest modulation on the electronic structure of Co_9S_8 by vanadium doping for high-performance rechargeable Zn–air batteries, Appl. Catal. B-Environ. 324 (2023) 122250, https://doi.org/10.1016/j.apcatb.2022.122250.
[6] Y. Lu, H. Zhang, W.C. Han, J.G. Zheng, H. Huang, L. Tao, B.G. An, L.X. Li, C.G. Sun, Multi-layered active sites attached in 1D/3D hierarchical conductive network promote dioxygen fragmentation, Appl. Surf. Sci. 638 (2023) 158099, https://doi.org/10.1016/j.apsusc.2023.158099.
[7] S.X. Li, H. Zhang, L. Wu, H.W. Zhao, L.X. Li, C.G. Sun, B.G. An, Vacancy-engineered CeO_2/Co heterostructure anchored on the nitrogen-doped porous carbon nanosheet arrays vertically grown on carbon cloth as an integrated cathode for the oxygen reduction reaction of rechargeable Zn–air battery, J. Mater. Chem. A 10 (2022) 9858–9868, https://doi.org/10.1039/D2TA01188C.
[8] L. Álvarez-Manuel, C. Alegre, D. Sebastián, A. Eizaguerri, P.F. Napal, M.J. Lázaro, N-doped carbon xerogels from urea-resorcinol-formaldehyde as carbon matrix for Fe-N-C catalysts for oxygen reduction in fuel cells, Catal. Today 418 (2023) 114067, https://doi.org/10.1016/j.cattod.2023.114067.
[9] A. Kobayashi, T. Fujii, K. Takeda, K. Tamoto, K. Kakinuma, M. Uchida, Effect of Pt loading percentage on carbon blacks with large interior nanopore volume on the performance and durability of polymer electrolyte fuel cells, ACS Appl. Energ. Mater. 5 (2022) 316–329, https://doi.org/10.1021/acsaem.1c02836.
[10] Y. Peng, J. Choi, L. Tian, K. Bai, Y. Zhang, D. Chen, J. Zeng, D. Banham, Impact of Pt spatial distribution on the relative humidity tolerance of Pt/C catalysts for fuel cell applications, J. Power Soruces. 545 (2022) 231906, https://doi.org/10.1016/j.jpowsour.2022.231906.
[11] H.C. Yang, N.D. Lu, J.T. Zhang, R. Wang, S.H. Tian, M.J. Wang, Z.X. Wang, K. Tao, F. Ma, S.L. Peng, Ultra-low single-atom Pt on g-C3N4 for electrochemical hydrogen peroxide production, Carbon Energy 5 (2023) e337, https://doi.org/10.1002/cey2.337.
[12] T.T. Hu, C.H. Chen, Y.B. Liu, L.X. Gong, Z.Q. Jiang, D. Bhalothia, T. Maiyalagan, Z. J. Jiang, Plasma-induced formation of Pt nanoparticles with optimized surface oxidation states for methanol oxidation and oxygen reduction reactions to achieve high-performance DMFCs, Small 19 (2023) 2304076, https://doi.org/10.1002/smll.202304076.
[13] K. Eid, A.A. Abdelhafiz, S. Abdel-Azeim, R.S. Varma, M.F. Shibl, Scalable nitrogen-enriched porous sub-100 nm graphitic carbon nanocapsules for efficient oxygen reduction reaction in different media, Green. Chem. (17) (2023) 6748–6758, https://doi.org/10.1039/D3GC01790G.
[14] X. Duan, F. Cao, R. Ding, X. Li, Q. Li, R. Aisha, S. Zhang, K. Hua, Z. Rui, Y. Wu, J. Li, A. Li, J. Liu, Cobalt-doping stabilized active and durable sub-2 nm Pt nanoclusters for low-Pt-loading PEMFC cathode, Adv. Energy Mater. 12 (2022) 2103144, https://doi.org/10.1002/aenm.202103144.
[15] N. Bhuvanendran, S. Ravichandran, K. Peng, Q. Xu, L. Khotseng, H. Su, Aminoclay/MWCNT supported spherical Pt nanoclusters with enhanced dual-functional electrocatalytic performance for oxygen reduction and methanol oxidation reactions, Appl. Surf. Sci. 565 (2021) 150511, https://doi.org/10.1016/j.apsusc.2021.150511.
[16] L. Liang, H. Jin, H. Zhou, B. Liu, C. Hu, D. Chen, J. Zhu, Z. Wang, H. Li, S. Liu, D. He, S. Mu, Ultra-small platinum nanoparticles segregated by nickle sites for efficient ORR and HER processes, J. Energy Chem. 65 (2022) 48–54, https://doi.org/10.1016/j.jechem.2021.05.033.
[17] H. Cheng, Z. Cao, Z. Chen, M. Zhao, M. Xie, Z. Lyu, Z. Zhu, M. Chi, Y. Xia, Catalytic system based on sub-2 nm Pt particles and its extraordinary activity and durability for oxygen reduction, Nano Lett. 19 (2019) 4997–5002, https://doi.org/10.1021/acs.nanolett.9b01221.
[18] M.G. Zhou, M.H. Liu, Q.Y. Miao, H.F. Shui, Q. Xu, Synergetic Pt atoms and nanoparticles anchored in standing carbon-derived from covalent organic frameworks for catalyzing ORR, Adv. Mater. Interface 9 (2022) 2201263, https://doi.org/10.1002/admi.202201263.

[19] W.J. Zhang, X. Feng, Z.X. Mao, J. Li, Z.D. Wei, Stably immobilizing sub-3 nm high-entropy Pt alloy nanocrystals in porous carbon as durable oxygen reduction electrocatalyst, Adv. Funct. Mater. 32 (2022) 2204110, https://doi.org/10.1002/adfm.202204110.
[20] L. Yang, R. Luo, X. Wen, Z. Liu, Z. Fei, L. Hu, Nanoconfinement effects of Ni@CNT for efficient electrocatalytic oxygen reduction and evolution reaction, J. Alloy. Compd. 897 (2022) 163206, https://doi.org/10.1016/j.jallcom.2021.163206.
[21] F. Tang, W. Xia, H. Zhang, L. Zheng, Y. Zhao, J. Ge, J. Tang, Synthesis of Fe-doped carbon hybrid composed of CNT/flake-like carbon for catalyzing oxygen reduction, Nano Res. 15 (2022) 6670–6677, https://doi.org/10.1007/s12274-022-4223-8.
[22] G. Singla, S.N. Bhange, M. Mahaian, S. Kurungot, Facile synthesis of CNT interconnected PVP-ZIF-8 derived hierarchically porous Zn/N co-doped carbon frameworks for oxygen reduction, Nanoscale 13 (2021) 6248–6258, https://doi.org/10.1039/D0NR09156A.
[23] W. Jiang, Y. Li, Y. Xu, T. Jiang, M. Zhao, M. Deng, R. Wu, Y. Wang, Carbon nanotube-bridged N-doped mesoporous carbon nanosphere with atomic and nanoscaled M (M = Fe, Co) species for synergistically enhanced oxygen reduction reaction, Chem. Eng. J. 421 (2021) 129689, https://doi.org/10.1016/j.cej.2021.129689.
[24] T. Ebbesen, H. Lezec, H. Hiura, J. Bennett, H. Ghaemi, T. Thio, Electrical conductivity of individual carbon nanotubes, Nature 382 (1996) 54–56, https://doi.org/10.1038/382054a0.
[25] Z. Shen, J. Du, Y. Mo, A. Chen, Nanocomposites of reduced graphene oxide modified with mesoporous carbon layers anchored by hollow carbon spheres for energy storage, Carbon 173 (2021) 22–30, https://doi.org/10.1016/j.carbon.2020.10.087.
[26] G. Liu, X. Xia, C. Zhao, X. Zhang, W. Zhang, Ultrafine Ni nanoparticles anchored on carbon nanofibers as highly efficient bifunctional air electrodes for flexible solid-state zinc-air batteries, J. Colloid Interface Sci. 588 (2021) 627–636, https://doi.org/10.1016/j.jcis.2020.11.053.
[27] M. Zhang, H. Li, J. Chen, F. Ma, L. Zhen, Z. Wen, C. Xu, Transition metal (Co, Ni, Fe, Cu) single-atom catalysts anchored on 3D nitrogen-doped porous carbon nanosheets as efficient oxygen reduction electrocatalysts for Zn–air battery, Small 18 (2022) 2202476, https://doi.org/10.1002/smll.202202476.
[28] B. An, S. Xu, L. Li, J. Tao, F. Huang, X. Geng, Carbon nanotubes coated with a nitrogen-doped carbon layer and its enhanced electrochemical capacitance, J. Mater. Chem. A 1 (2013) 7222, https://doi.org/10.1039/C3TA10830A.
[29] Y. Han, Y. Wang, W. Chen, R. Xu, L. Zheng, J. Zhang, J. Luo, R. Shen, Y. Zhu, W. Cheong, C. Chen, Q. Peng, D. Wang, Y. Li, Hollow N-Doped carbon spheres with isolated cobalt single atomic sites: superior electrocatalysts for oxygen reduction, J. Am. Chem. Soc. 139 (2017) 17269–17272, https://doi.org/10.1021/jacs.7b10194.
[30] L. Tao, D. Dastan, W.S. Wang, P. Poldorn, X.Z. Meng, M.J. Wu, H.W. Zhao, H. Zhang, L.X. Li, B.G. An, Metal-decorated InN monolayer senses N_2 against CO_2, ACS Appl. Mater. Interfaces 15 (2023) 12534–12544, https://doi.org/10.1021/acsami.2c21463.
[31] X. Yan, B. Tay, Y. Yang, W. Po, Fabrication of three-dimensional ZnO−carbon nanotube (CNT) hybrids using self-assembled CNT micropatterns as framework, J. Phys. Chem. C. 111 (2007) 17254–17259, https://doi.org/10.1021/jp076064e.
[32] A. Bharti, G. Cheruvally, S. Muliankeezhu, Microwave assisted facile synthesis of Pt/CNT catalyst for proton exchange membrane fuel cell application, Int. J. Hydrog. Energy 42 (2017) 11622–11631. ⟨https://doi.org/10.1039/B9NR00140A⟩.
[33] R. Tang, K. Taguchi, H. Nishihara, T. Ishii, E. Morallón, D. Cazorla-Amorós, T. Asada, N. Kobayashi, Y. Muramatsu, T. Kyotani, Insight into the origin of carbon corrosion in positive electrodes of supercapacitors, J. Mater. Chem. A 7 (2019) 7480–7488, https://doi.org/10.1039/C8TA11005K.
[34] H. Nishihara, H. Zhao, K. Kanamaru, K. Nomura, M. Ohwada, M. Ito, L. Li, B. An, T. Horikawa, T. Kyotani, Adsorption properties of templated nanoporous carbons consisting of 1-2 graphene layers, Carbon Rep. 1 (2022) 123–135, https://doi.org/10.7209/carbon.010301.
[35] Y.L. Jiang, P.F. Wang, T.Y. Chen, K.Y. Gao, Y.R. Xiong, Y. Lu, D.D. Dionysiou, D. W. Wang, Efficient $^1O_2$ production from H_2O_2 over lattice distortion controlled spinel ferrites, Appl. Catal. B-Environ. Energy 353 (2024) 124057, https://doi.org/10.1016/j.apcatb.2023.123468.
[36] Q. Liang, W. Li, L. Xie, Y. He, B. Qiu, H. Zeng, S. Zhou, J. Zeng, T. Liu, M. Yan, K. Liang, O. Terasaki, L. Jiang, B. Kong, General synergistic capture-bonding superassembly of atomically dispersed catalysts on micropore-vacancy frameworks, Nano Lett. 22 (2022) 2889–2897, https://doi.org/10.1021/acs.nanolett.2c00042.
[37] H. Jiang, J. Xia, L. Jiao, X. Meng, P. Wang, C.-S. Lee, W. Zhang, Ni single atoms anchored on N-doped carbon nanosheets as bifunctional electrocatalysts for Urea-assisted rechargeable Zn-air batteries, Appl. Catal. B-Environ. 310 (2022) 121352, https://doi.org/10.1016/j.apcatb.2022.121352.
[38] Y.L. Jiang, P.F. Wang, Y.R. Xiong, T.Y. Chen, C. Zhang, K.Y. Gao, X.G. Duan, D. W. Wang, Perovskite manganese oxides with tunable metal–oxygen covalency for efficient bisphenol A degradation, J. Mater. Chem. A 11 (2023) 26707–26715, https://doi.org/10.1039/D3TA06135C.
[39] W. Xia, M. Hunter, J. Wang, G. Zhu, S. Warren, Y. Zhao, Y. Bando, D. Searles, Y. Yamauchi, J. Tang, Highly ordered macroporous dual-element-doped carbon from metal-organic frameworks for catalyzing oxygen reduction, Chem. Sci. 11 (2020) 9584–9592, https://doi.org/10.1039/D0SC02518F.
[40] W. Yang, X. Liu, X. Yue, J. Jia, S. Guo, Bamboo-like carbon nanotube/Fe_3C nanoparticle hybrids and their highly efficient catalysis for oxygen teduction, J. Am. Chem. Soc. 137 (2015) 1436–1439, https://doi.org/10.1021/ja5129132.
[41] L. Liang, H. Jin, H. Zhou, B. Liu, C. Hu, D. Chen, Z. Wang, Z. Hu, Y. Zhao, H.-W. Li, D. He, S. Mu, Cobalt single atom site isolated Pt nanoparticles for efficient ORR and HER in acid media, Nano Energy 88 (2021) 106221, https://doi.org/10.1016/j.nanoen.2021.106221.
[42] J. Ma, A. Habrioux, Y. Luo, G. Ramos-Sanchez, L. Calvillo, G. Granozzi, P. B. Balbuena, N. Alonso-Vante, Electronic interaction between platinum nanoparticles and nitrogen-doped reduced graphene oxide: effect on the oxygen reduction reaction, J. Mater. Chem. A 3 (2015) 11891–11904, https://doi.org/10.1039/C5TA01285F.